COMBINED TRANSDUCER AND NONLINEAR TISSUE PROPAGATION SIMULATIONS

Gregory L. Wojcik, John C. Mould Jr., Laura M. Carcione

Weidlinger Associates, Inc.

4410 El Camino Real, Suite 110, Los Altos, CA 94022-1049

ABSTRACT

Ultrasonic imaging system evaluation is often based on models of the transducer as a distribution of baffled piston sources, and of the tissue as a homogeneous, linear acoustic medium, e.g., Jensen's Field code. In reality, these are fairly gross idealizations, since the transducer exhibits more complicated response modes and real tissue is inhomogeneous and nonlinear. Greater model fidelity would be useful, especially in the context of transducer design qualification, second harmonic imaging, and acoustic power indices. To this end we combine 2D finite element models of transducer dynamics with highly accurate 2D finite difference propagation models in the large-scale inhomogeneous tissue cross-sections. Transducer models employ the time-domain code, PZFlex, and tissue models utilize a new pseudospectral solver to be included in PZFlex. The pseudospectral algorithm solves the inhomogeneous acoustic wave equation using FFTs for high order approximation of the spatial differential operator and a fourth-order, explicit time integrator. Second-order (B/A) nonlinearity and frequency-accurate, causal absorption are included. We describe the algorithmic and modeling issues, and present a suite of simulations in lossy, nonlinear abdominal cross sections and tissue showing coupling of the 1D medical array to the tissue model and scattering from deeper inhomogeneities and back to the transducer. In contrast to paraxial schemes, like the KZK method, details of the field transmitted from the transducer and all backscatter within the model are included. However, models are currently limited to 2D (plane or axisymmetric) on readily available hardware.

Key Words: Imaging, transducers, tissue, simulations, aberrations, finite elements, pseudospectral, scattering, second harmonic, acoustic power

INTRODUCTION

There are compelling clinical and economic reasons for studying the interaction of actual medical transducer pulses with real tissue structure. One is, of course, the pulse distortion or aberration caused by superficial tissue structure, e.g., skin, fat, and muscle, which reduces contrast and lateral resolution of medical ultrasonic imaging systems. Another is the acoustic power issue, e.g., mechanical and thermal indices, for insuring that ultrasonic bioeffects are negligible, as well as to comply with FDA regulations. Experimental study in living tissue is not practical, in general, and acoustic phantoms are useful but limited. Mathematical computer modeling of ultrasound propagation and scattering is an attractive complement to both approaches, although it has its own set of limitations.

"First-order" mathematical models represent the transducer as a distribution of baffled piston sources driving a homogeneous, linear acoustic medium representing the tissue. In practice, these diffraction theory models are too idealized, since the transducer generally exhibits element cross-talk and spurious modes, while more to the point, real tissue is inhomogeneous and nonlinear. Clearly, less idealization would be useful, particularly in the context of advanced transducer designs and materials, aberration correction schemes, second harmonic imaging, and thermal/mechanical index estimation. However, including the necessary structural and constitutive details complicates the model problem enormously, to the point that no known numerical schemes are able to provide comprehensive simulations.

Difficulties with higher-order modeling include three-dimensional (3D) geometrical and material complexity and very large scale, combined with fundamental limitations of the available numerical algorithms. In particular, the source/transducer region comprises active and passive elastic materials, beyond which the acoustic propagation paths are many hundreds of wavelengths through heterogeneous, nonlinear tissue with multiple structural scales. Backscatter from coherent tissue structure is, of course, the field quantity of principal interest. Among the available numerical options, KZK-type schemes are based on the paraxial (one way) wave equation approximation, which specifically excludes the backscattered component, while more complete finite difference or finite element algorithms are not accurate over the very long propagation paths of interest.

A variety of first-order imaging models have been developed by both academic and industry researchers. Industry efforts are typically proprietary, but most academic work has been reported in the literature. In particular, Jensen and coworkers[1] describe medical imaging simulations and Hayward's group[2] reports on a simulator for underwater sonar imaging. Both approaches represent ultrasonic transducers by a discrete number of baffled "piston" sources of rectangular or triangular shape. On this basis, classical diffraction theory is used to calculate radiated acoustic fields via boundary integral representations of spatial impulse response (Green's functions). For example, Jensen utilizes the approach suggested by Tupholme[3] and Stepanishen[4]. Despite the maturity of boundary integral representations (often associated with the names of Kirchhoff and Helmholtz) there is still a need for improved computational algorithms to handle the large number of source and receiver points. Backscatter from an insonified object is calculated by approximating the object by discrete point diffractors representing volume scatterers (Jensen) or line diffractors representing edges of artificial structures (Hayward).

These first-order models are limited less by the transducer representation than by the homogeneous, linear medium assumption required for "closed form" wave propagation solutions. Homogeneity in an underwater environment is usually a reasonable idealization. This is not the case in medical imaging, e.g., through the abdominal wall or ribcage. Therefore, the starting point for generalizing a first-order

imaging scheme is introduction of a heterogeneous tissue propagation model. This means that classical Green's functions and integral wave representations must be replaced by discrete numerical methods. If there are a small number of clear interfaces then boundary integral methods are an option. In general, however, "brute force" discrete methods are necessary, utilizing either finite element[5] (FE) or finite difference[6] (FD) approximations of the acoustic wave equation's spatial operator.

The difficulty with discrete modeling methods for imaging is the long propagation distance. For example, over a 10 cm round-trip or direct travel path, 5 MHz waves propagate 333 wavelengths. At these ranges, typical FE or FD algorithms distort signals unacceptably because they use local, low order space and time derivative approximations to achieve modeling versatility and computational efficiency, rather than ultimate numerical accuracy. Long range wave distortion is caused by artificial spatial and temporal sampling that make numerical phase velocity and attenuation depend on direction and frequency. Figure 1 illustrates 1D wave solutions that are 2nd order accurate in space (FE or FD) and time (central difference). A wavelet is initialized at one end of a long model and propagated past a point 300 wavelengths away, using a practical spatial sampling of 20 elements/wave at the wavelet's center frequency with timestep $\Delta t=0.99\Delta x/c$ and $\Delta t=0.8\Delta x/c$. Δx is spatial interval, c is continuum wavespeed, and the numerical coefficient is the so-called Courant stability factor for the grid. The smaller stability factor, 0.8, is a typical value for heterogeneous tissue, but spatial and temporal errors compromise the wavelet unacceptably at this range. Fourier transforms of these waveforms show identical amplitude spectra, so pulse distortion is due to phase errors, i.e., dispersion, not numerical damping.
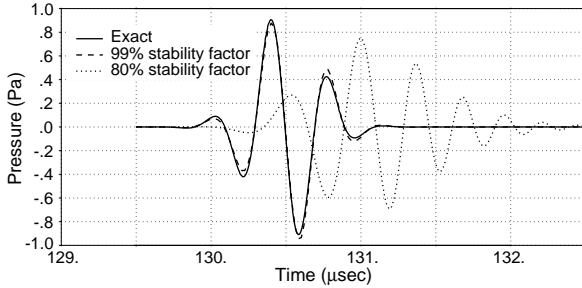
Figure 1. Crossplot of wavelet time histories after traveling 300 wavelengths in a 1D, 2nd order accurate grid (FE or FD).

To provide a more accurate and comprehensive alternative, this paper presents a two-dimensional (2D) hybrid scheme that combines structurally detailed FE models of the transducer with large-scale, highly accurate FD models of the inhomogeneous tissue cross-section. The transducer models employ a time-domain finite element code, PZFlex, and the tissue models utilize a pseudospectral finite difference solver included in the PZFlex package[7,8]. The pseudospectral algorithm[9] solves the inhomogeneous acoustic wave equation using the fast Fourier transform (FFT) to evaluate spatial derivatives to very high order. Time is advanced step-by-step using a fourth-order, explicit time integrator. Material nonlinearity is included in the constitutive relations, along with causal attenuation models based on multiple relaxation mechanisms.

This combination of comprehensive transducer and tissue models represents a new capability and provides novel insights and interpretations. We describe the algorithms and modeling issues, and present a suite of simulations in lossy, nonlinear abdominal cross sections and deeper tissue, showing coupling of the fully characterized 1D medical array to the tissue model. Realistic models of abdominal wall morphology are critical to aberration studies. Careful measurements of

abdominal wall sections by Hinkelman[10,11] are the basis for the following model studies. These simulations graphically illustrate wave front aberrations, general scattering, and second harmonic generation as a function of tissue (absorption, B/A) and transducer properties (intensity, focus, cross-talk). The results permit quantification of wave front distortion and scattering for evaluating aberration correction schemes, and to contrast first and second harmonic beam properties.

THE ACOUSTIC WAVE SOLVER

To simulate ultrasound in tissue models we solve the governing partial differential equations (PDEs). Linear forms are given by the conventional momentum and constitutive equations,

$$\rho\frac{\partial^2 u}{\partial t^2} = -\nabla p \quad , \quad p = -K\nabla \cdot u \tag{1}$$

where $u=(u_x, u_y, u_z)^T$ is the displacement vector, p is pressure, ρ is density, $K=\rho c^2$ is bulk modulus, and c is wavespeed. Coefficients ρ, K, and c are functions of space. Eliminating p in (1) yields the wave equation on u, however, spatial derivatives of ρ and c appear through $\nabla K=c^2\nabla\rho+2\rho c\nabla c$. Alternately, differentiating the constitutive equation with respect to time yields the first order system on velocity vector $v=(v_x,v_y,v_z)^T$ and pressure,

$$\frac{\partial v}{\partial t} = -\frac{1}{\rho}\nabla p \quad , \quad \frac{\partial p}{\partial t} = -K\nabla \cdot v \tag{2}$$

which does not involve explicit derivatives of coefficients.

The discrete, 2D form of (2) is written by sampling velocity and pressure on the $N = N_x \times N_y$ points of a Cartesian grid. Defining N-vectors on velocities V_x, V_y and pressure P, the system of discrete equations is

$$\frac{\partial W}{\partial t} = f(W) \quad , \quad W \equiv \left(V_x, V_y, P\right)^T \quad ,$$

$$f(W) = \left(-\frac{1}{\rho}\frac{\partial p}{\partial x}, -\frac{1}{\rho}\frac{\partial p}{\partial y}, -K\left(\frac{\partial V_x}{\partial x}+\frac{\partial V_y}{\partial y}\right)\right)^T \tag{3}$$

where W is the work vector of length 3N and the T superscript denotes the transpose.

The discrete acoustic wave equation (3) is reduced to a system of ordinary differential equations (ODEs) by evaluating the spatial derivatives. Time-domain numerical solutions of these ODEs involve step-by-step integration in time and evaluation of spatial derivatives at each step. Solutions must include radiation boundary conditions, nonlinearity, and frequency-dependent absorption.

THE PSEUDOSPECTRAL METHOD

The periodic pseudospectral method uses discrete Fourier transforms to evaluate spatial derivatives of functions defined on a uniform Cartesian grid. On this basis, time-dependent PDEs are reduced to ODEs, which are integrated forward in time using either explicit or implicit methods. As with FD and FE methods, the PS gridpoints must be dense enough to resolve spatial details of the PDE coefficients over the domain. However, unlike uniform difference stencils or element meshes, the PS method is global and yields a very high order spatial derivative approximation, equal to the number of grid points in each direction[9], e.g., N_x and N_y.

Recall that if $\hat{u}(k)$ is the Fourier transform of u(x) with spatial frequency (transform parameter) k, then the derivative of $u(x)$ is the inverse Fourier transform of $jk\hat{u}(k)$, where $j=\sqrt{-1}$. Therefore, calculation

of the first derivative on a gridline of N points by the periodic PS method is done in three steps[9]: do a complex FFT on gridpoint data values, giving

$$\hat{u}_0 \ \hat{u}_1 \ \hat{u}_2 \ \cdots \ \hat{u}_{N/2-1} \ \hat{u}_{N/2} \ \hat{u}_{N/2+1} \ \cdots \ \hat{u}_{N/2-2} \ \hat{u}_{N-1}$$

multiply these output elements by discrete spatial frequencies

$$0 \ \pi j \ 2\pi j \cdots (N/2-1)\pi j \ 0 \ -(N/2-1)\pi j \cdots -2\pi j \ -\pi j;$$

and perform a complex inverse FFT on the result. This yields the PS derivative approximation at the gridpoints. Since the procedure gives a real derivative from real data and the complex FFT is linear, we can initialize the real and imaginary parts of the FFT input with two independent real data sets and recover derivatives of each in the real and imaginary outputs. Note that the practical disadvantage of this method is spatial periodicity, which exhibits itself as "wraparound" of the field.

The PS method provides an extremely accurate approximation of spatial derivatives in homogeneous media on a uniform, periodic FD mesh, even at 2 nodes per wavelength. Of course, analytical, i.e., "nodeless," solutions can always be constructed in homogeneous media, so high numerical accuracy with coarse sampling should not come as a surprise. Numerical errors are introduced at material interfaces and within distributed inhomogeneities. These are reduced by staggering the PS grid in space[12], i.e., defining pressures and velocities at interlaced points. This is in contrast to the easier, nonstaggered implementation. The difference is that local errors decay as $1/r$ in the nonstaggered grid, but as $1/r^2$ in the staggered grid[9]. Accuracy gains more than offset implementation difficulties of staggered grids. For the low contrasts typical of soft tissue, numerical experiments show that staggered PS spatial derivatives are adequate at 4-5 nodes per wavelength, but results do depend on the level of contrast, e.g., soft to hard tissue.

On this basis, the solution algorithm for hyperbolic system (3) over one timestep Δt is: load new values of V_x, V_y, P into W; calculate spatial derivatives of V_x, V_y, P on gridlines; evaluate $dW/dt = f(W)$ and integrate the system one timestep. This sequence must be repeated as many times as necessary to capture the wave phenomena of interest. There are many effective integrators available, both implicit and explicit. The unconditional stability (i.e., any Δt) of implicit schemes is wasted for the present wave applications since timestep is controlled by accuracy requirements. Implicit schemes also require solutions of matrix equations that are prohibitively expensive for large-scale problems. For accurate time-domain calculations, explicit time integrators are best.

Our first PS version[7] used the 4th order Runge Kutta integrator (RK4), which is robust, convenient and reasonably accurate. 2nd order methods like leapfrog were unacceptable for long-range propagation. It was noted that the 4th order Adams Bashforth integrator offered advantages. Recent work by Ghrist et al.[13] showed that staggering (evaluating velocity at full time steps and pressure at half time steps) the 4th order Adams Bashforth integrator, referred to as ABS4, improved both accuracy and stability relative to RK4. Surprisingly, ABS4 was also shown[8] to yield a factor of 4-6 reduction in parallel computation time relative to RK4. All calculations described below utilize ABS4, with starting values obtained from a RK4 step of ½Δt.

BERENGER'S PERFECTLY MATCHED LAYER (PML)

The price for high PS spatial accuracy is a space-periodic domain. Thus, solutions exhibit wraparound at the boundaries, i.e., waves effectively exit one side and enter the opposite side. Berenger's PML boundary condition[14] is used to circumvent wraparound by forcing the solution to be "periodically small" at the boundaries. Berenger[14] showed how to construct the wave equation for a nonphysical medium that is highly attenuative yet nonreflective at any angle of incidence. The objective was efficient radiation boundary conditions for FD grids, in the context of wave equations for TE and TM electromagnetic field polarizations. Therefore, his approach is directly applicable to the acoustic wave equation (but not to the vector elasticity equations).

An acoustic PML implementation for 2nd order, FD, time-domain solvers is described by Yuan, et. al.[15], who demonstrated that waves incident from the grid's interior on an eight-node boundary layer are rapidly absorbed, with spurious reflections reduced by 80 dB. One way to write the acoustic analog to Berenger's electromagnetic PML is to split pressure p into $p=p_x+p_y+p_z$ and introduce anisotropic attenuation coefficients α_x, α_y, α_z. The 2D acoustic PML equations then become

$$\frac{\partial v_x}{\partial t} = -\frac{1}{\rho}\frac{\partial p}{\partial x} - K\alpha_x v_x \quad , \quad \frac{\partial v_y}{\partial t} = -\frac{1}{\rho}\frac{\partial p}{\partial y} - K\alpha_y v_y$$

$$\frac{\partial p_x}{\partial t} = -K\frac{\partial v_x}{\partial x} - K\alpha_x p_x \quad , \quad \frac{\partial p_y}{\partial t} = -K\frac{\partial v_y}{\partial y} - K\alpha_y p_y \tag{4}$$

These can replace acoustic equations (2) everywhere, with $\alpha_x=\alpha_y=0$ in the interior and nonzero near the boundaries. For computational efficiency, however, (4) should only be applied in a layer near the boundary. Smoothly increasing attenuation through this layer turns out to be optimal in order to absorb small reflections introduced by discretization of the continuum PML equations.

In the present case eight nodes near the boundary are "activated," i.e., have nonzero α. The problem remains periodic but "periodically small" at the boundaries, i.e. field values are driven towards zero there by the PML. Wraparound causes signals to do a double pass through the absorber, e.g., as an outgoing wave enters the PML on one side it is attenuated and any signal reaching the boundary enters the PML at the opposite boundary where it is further attenuated.

ATTENUATION AND NONLINEARITY

Wave attenuation is an essential part of tissue models. There are various attenuation mechanisms, including shear and bulk viscosities, a multiplicity of relaxation phenomena, and wave scattering. Since few of these mechanisms can be isolated, aggregate attenuation is measured and characterized by a power law in frequency f as $\alpha=af^b$. For example, in water a ≈ 0.0022 dB/cm/MHz^b, b=2.0, and in muscle tissue a ≈ 0.7 dB/cm/MHz^b, b ≈ 1.1. Theories and implementations range from computationally simple stiffness and mass proportional damping to viscoacoustic and related dispersion formulations[16-18] familiar from classical electromagnetic theory for lossy dielectrics. Note that stiffness proportional damping is ideal in water. The general viscoacoustic case[17] is implemented here, with multiple relaxation frequencies used to accurately model power law frequency dependence. A least squares procedure chooses model parameters for an optimal fit over a specified frequency range. Two mechanisms are adequate over the 2-6 MHz range considered here. This is illustrated in Fig. 2, showing fits to power laws with exponents 0.6, 1.0 and 1.4.
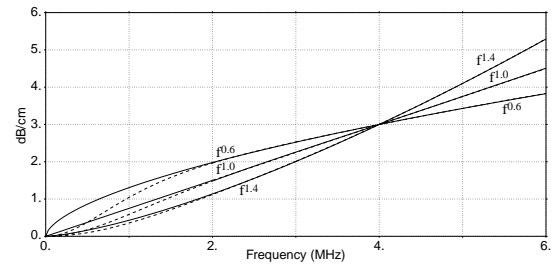

Figure 2. Least squares fits of attenuation power laws from 2 to 6 MHz using two relaxation frequencies.

Harmonic distortion due to weak shock effects, i.e., material nonlinearity, is also an essential aspect of tissue models. In 1980 Muir and Carstensen[18] first demonstrated that conventional imaging arrays produced significant nonlinear effects. The appropriate nonlinear wave equation follows by generalizing the pressure-density (constitutive) relation in (1). Expanding pressure in a power series and retaining the first two terms yields the widely accepted "B/A" model, namely,

$$p = -K\left(\nabla \cdot u + \frac{1}{2}\frac{B}{A}(\nabla \cdot u)^2 \right) \qquad (5)$$

where K is the bulk modulus. This is implemented in the current PS solver. Other nonlinear models, e.g., more general power laws, are easily incorporated, but the third order differences with the B/A model are not of concern here. Note that accurate tissue absorption is a necessary complement to nonlinear modeling. Otherwise unphysical harmonic generation rapidly exceeds the resolution of any discrete grid.

Harmonic generation, i.e., shocking, is particularly impressive in water, where absorption is less than 1% that of tissue. For example, Fig. 3 shows water pulse measurements from an Acuson linear array[8] with 7 cm fixed elevational focus. It is driven uniformly in azimuth by a 4-cycle RF signal with 2.5 MHz center frequency. Peak-to-peak pressure 2 mm from the lens is 1.3 MPa, which is a typical clinical value. The left graph in Fig. 3 shows pulse waveforms at 0.2, 5, and 6 cm (time shifted for plotting). Shocking is obvious towards the 7 cm elevation focus. The right graph is a cross-plot of amplitude spectra, showing strong harmonic generation (integer multiples), as well as interesting intermediate peaks. In tissue, less dramatic but significant second and third harmonics are generated at clinical drive levels.
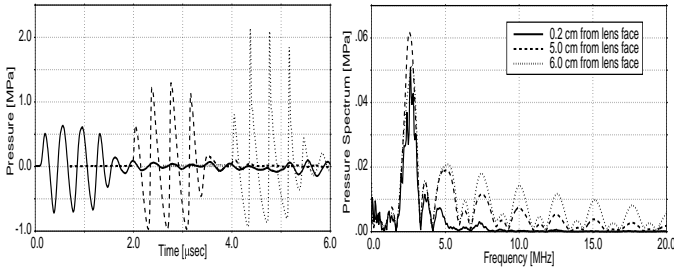

Figure 3. Experimental data showing harmonic generation in water by a 1D, fixed-focus medical array.
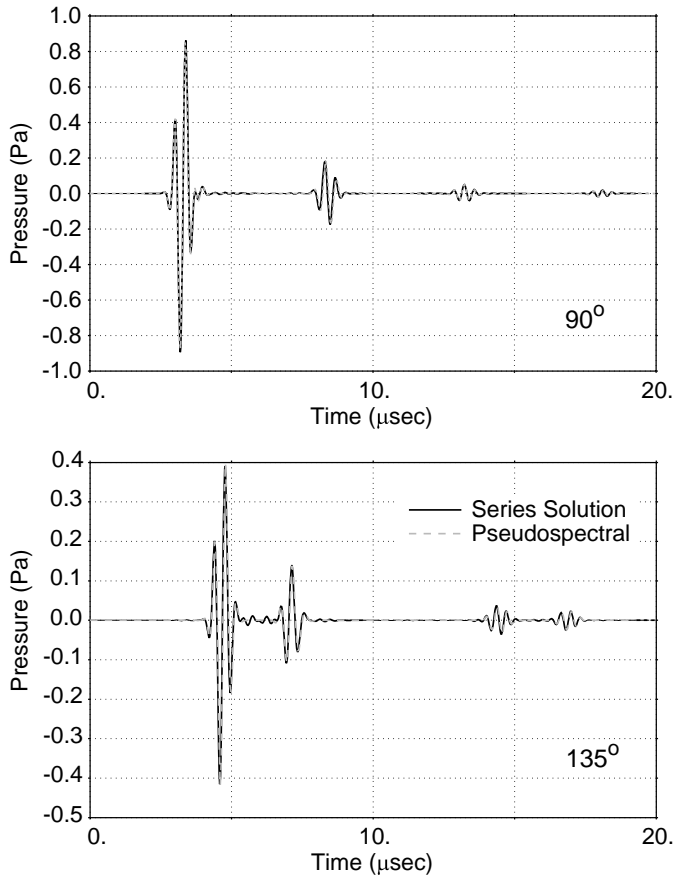
VALIDATION

To validate the PS method with Berenger's PML we consider scattering of a plane wave in water by a soft acoustic cylinder[7]. Diameter of the cylinder is 6 mm and its wavespeed is 1200 m/s, compared to 1500 m/s in water. A 256x256 PS-PML grid with nodal spacing of 58 microns is used in order to include initial wave conditions and capture spatial frequency content. The stairstep approximation of the cylinder interface is fairly refined, i.e., 100 nodes across the cylinder. The PS solution with a 4th order Runge-Kutta integrator is compared to a truncated series solution (analytical) at 45°, 90°, and 135° from the leading edge, on a 4 mm radius circle. These points are indicated in Fig. 4, which was calculated without (top) and with (bottom) the PML, illustrating wraparound and its effective removal. Cross-plotting model and numerical results yields the excellent agreement in Fig. 5. Discernible phase errors are due to output location mismatch, i.e., grid points closest to the specified output coordinate. In general, the PML condition works very well and noise for this implementation is 100 dB below the input.
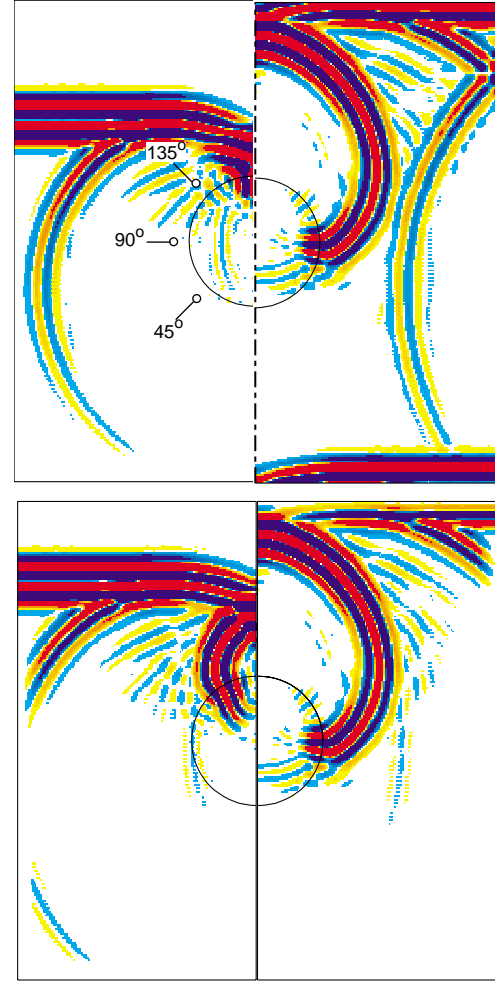
Figure 4. Composite pictures illustrating plane wave scattering by a slower cylinder in water, using the 2D PS/Runge-Kutta method. The top composite shows before (left) and after (right) wraparound of the scattered wave. The bottom composite shows similar snapshots but with the PML treatment, demonstrating elimination of wraparound at the periodic boundaries.
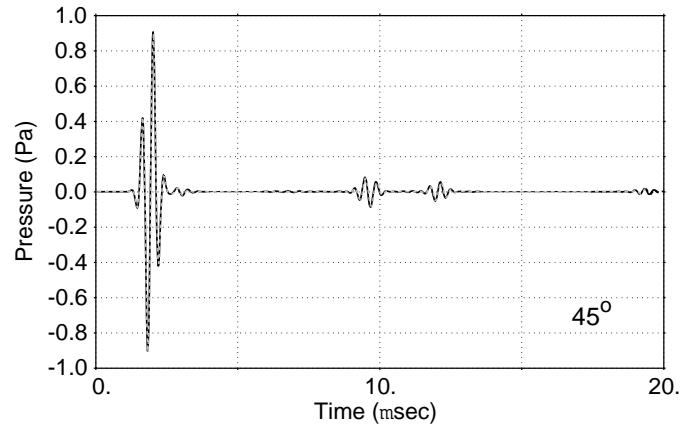

Figure 5. Validation of the PS method and PML against a truncated series solution at the output points indicated in Fig. 4.

Figure 6. Example of PZFlex transducer calculation for initialization of pseudospectral propagation model. The model consists of 64 elements in a subdiced 1D array[24], each driven with a voltage pulse delayed for 5 cm focus. Two elements of the subdiced array model are shown above and include backing, two matching layers and a water load.

Figure 5. Validation of the PS method and PML against a truncated series solution at the output points indicated in Fig. 4. (continuation)

INITIALIZATION

There are no boundaries in the PS space domain—only periodicity. Therefore, in the absence of conventional boundaries, waves are necessarily introduced as initial conditions. Alternatively, we can consider introducing an internal boundary condition, i.e., initializing the wave field on single space line for all time. This type of internal discontinuity is only practical with the staggered grid described earlier, due to localization of errors.

Unidirectional wave motion is initiated by two initial conditions, e.g., pressure *and* velocity. A single field initial condition yields waves traveling in "opposite" directions on the two characteristic surfaces in x,y,t space. The unwanted backward traveling wave is absorbed by the PML. The examples shown here were driven by initial conditions over the grid. However, we have demonstrated effectively the same results with an internal boundary condition.

The field distributions for initial or internal boundary conditions must be determined analytically, numerically, or experimentally. In practice we often want to apply a signal from an actual transducer design. This can be simulated numerically or measured in a water tank over the face of the transducer. An example of numerical initialization is illustrated in Figure 6. This shows a PZFlex calculation of a 1D, 5 MHz transducer array with each element driven by a time-delayed voltage pulse. Delays are chosen for a 5 cm focus. Two elements of the subdiced array model are also shown. In this way nonideal behavior of the transmitted field can be included in the large-scale wave simulation.
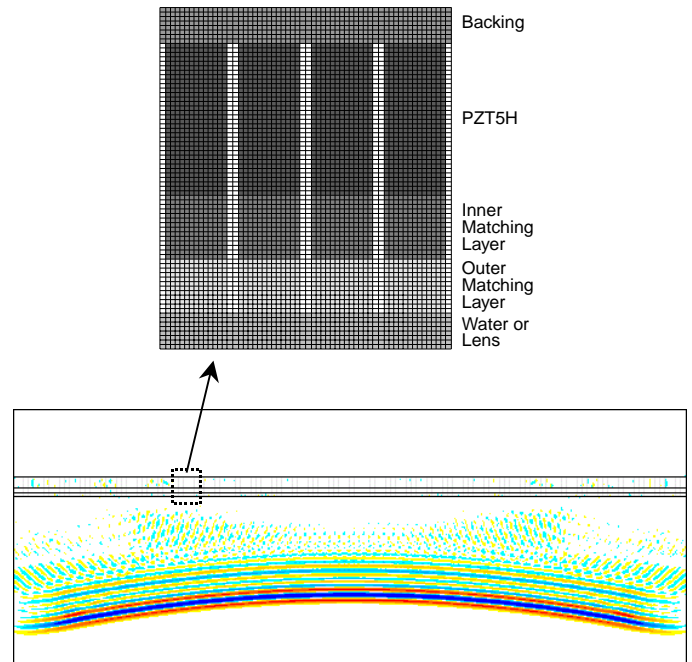
In principle, the internal boundary permits a smaller region for wave input to the PS calculation. More importantly, it provides a convenient input for experimental pressure data (time histories) measured over a line in front of the transducer. Work is in progress on internal boundary initialization from experimental data.

PARALLELIZATION

The relevant scales for large bioacoustic problems are, say, 0.3 mm waves (5 MHz) in a 10x10(x10) cm tissue model. Assuming 4 nodes/wave for the PS model yields 333x333(x333) wavelengths or ≈ 1.8 x 10^6 nodes in 2D (≈ 2.4 x 10^9 in 3D). To capture details of tissue structure or harmonics we can easily double or triple the number of nodes per wavelength. 2D models can reach tens of million of nodes and 3D models must be restricted to a very limited field to be practical. Therefore, parallel computing is an essential paradigm for large-scale models of ultrasound propagation. A PS parallel implementation of the RK4 integrator solved each equation in (4) on its own processor, with 65% parallel efficiency. For larger problems and additional processors, it is more efficient to parallelize the loops in the FFT and integration routines and run on a symmetric multiprocessing (SMP) machine. Current implementations yield SMP efficiencies of 60% to 80% on 6 of 8 available processors.

The PS algorithm described above yields an accurate, complete wave solver. Fine-tuning of the implementation is possible, but potential gains appear less than a factor of 5. Therefore, for current PCs and workstations, simulations of 300+ wavelength models are restricted to 2D. Fortunately, a great deal of information can be gained from 2D simulations. Similar 3D simulations are only feasible on a massively parallel machine with O(1000) processors. This requires distributed parallel processing. Parallelism is achieved by partitioning the computational volume rather than SMP. Domain decomposition has

been demonstrated[20] for the 3D pseudospectral algorithm. Therefore, 3D versions of our present examples are feasible on existing massively parallel systems. Development along these lines is currently being explored.
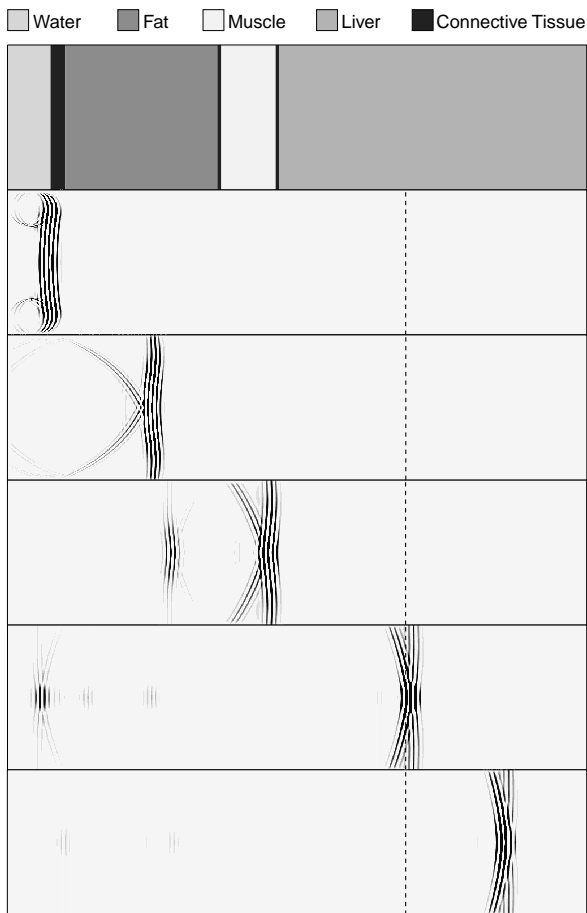
Figure 7a. Snapshots of pulse propagation through the piecewise homogeneous abdominal wall model (MS1).

LARGE-SCALE PROPAGATION IN TISSUE MODELS

To demonstrate efficacy of the algorithm and the variety of wave propagation phenomena to be expected, ultrasonic pulses are propagated through three abdominal wall model sections labeled MS1-MS3. MS1 is a piecewise homogenous approximation of abdominal wall section MS2, both shown in the top panel of Figure 7a,b. MS3 is similar to MS2 but with less fat marbling in the muscle, as shown in Figure 9b. Note that

Table 1. Material Properties

Tissue/ Material	ρ [kg/m³]	V [m/sec]	B/A	Loss [dB/ cm/MHz^b]	b
Water	1000	1500	5.0	0.002*	2.0
Fat	928	1427	10.0	0.75	1.0
Connective	1100	1537	7.87	1.125	1.0
Muscle	1041	1571	7.5	0.55	1.0
Liver	1050	1577	6.75	0.4	1.0

* set to zero in simulation

MS2 and MS3 are drawn from Hinkelman's[10,11] measurements of actual abdominal wall tissue cross-sections. Approximate material properties for the fat, muscle, liver, and connective tissue are given in Table 1, extracted from data reproduced in Duck[21]. The short water path was assumed linear and tissues were simulated with B/A (2nd order) nonlinearity and a two-mechanism relaxation model.

PULSE PROPAGATION

Pseudospectral calculations in MS1, MS2 and MS3 simulate a 2.5 MHz transducer with 1.5 cm aperture and 5 cm geometric focus. The pulse is generated by simply bending a plane wave to the appropriate radius of curvature and setting initial conditions on pressure and velocity in the water layer. Models are 2x8 cm with the PML on all sides. They are discretized at 256 x 1024 cells, producing a cell size of 0.0078125 cm, or 4 cells per wavelength at the second harmonic. The pulse is propagated through the model for 5000 timesteps at 20% of the Courant stability limit, chosen for accuracy rather than maximum allowable timestep. Simulations require about 2 hours each on an SGI Origin 2000, using 6 of the 8 available processors. Parallel efficiency is about 80%, i.e., simulations would have required 10 hours each on a single CPU.
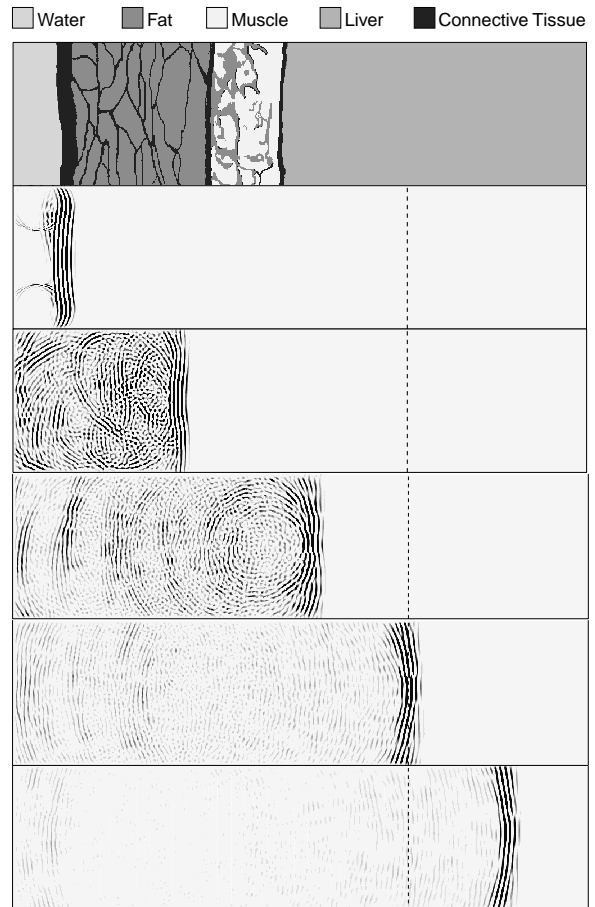

Figure 7b. Snapshots of pulse propagation through a typical abdominal wall model section (MS2) from Hinkelman's measurements[10,11].

Figure 7a,b illustrates the progression of a 2.5 MHz pulse through abdominal wall model sections MS1 (7a) and MS2 (7b). The dashed line indicates the geometric focus. In the first snapshot the wave has just

penetrated the skin. For graphical definition only pulse compression is plotted in greyscale. Circular diffracted waves from the edges of the insonified region are apparent. These edge diffractions are produced by any finite transducer, although details differ depending on aperture, phasing, housing, etc. In the third snapshot in MS1 note the reflections and diffractions from the muscle interface. The PML has accurately removed outgoing waves at the sides of the model with no spurious reflections. In the fourth snapshot, the pulse has reached the geometric focus. In MS2, the fine tissue structure produces considerable diffuse scattering relative to the idealized model, MS1. Dropouts or shadow regions are also evident in later snapshots.

Figure 8 compares the amplitude spectrum of the pulse at its geometric focus with that of the input signal (arbitrarily scaled). In MS1 a significant second harmonic at 5 MHz and a weaker, essentially undamped, sub-harmonic (rectified or DC pulse) near 0.5 MHz are apparent. The amplitude spectrum in MS2 is similar but reduced significantly by backscatter.
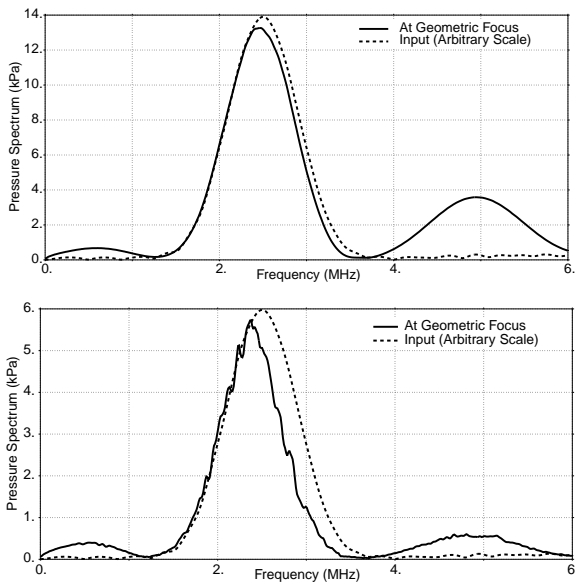

Figure 8. Amplitude spectrum of pulse at the geometric focus in piecewise homogeneous abdominal wall model (MS1) (top), and abdominal wall model (MS2) (bottom), compared to spectrum of scaled input pulse.

ABERRATION AND SECOND HARMONIC GENERATION

Computer simulations in realistic tissue models can provide useful information on the second harmonic generation and wavefront aberration processes. They require accurate solutions of the scalar (acoustic), full wave equation in large-scale, heterogeneous, lossy, nonlinear media. The subject pseudospectral code satisfies all of the above simulation requirements. Alternatively, the KZK and related methods[22,23] could be used. However, KZK-type methods are not as robust in inhomogeneous media and only capture forward and limited off-axis propagation due to the underlying paraxial (parabolic wave equation) basis. Omnidirectional solutions are important because of the fundamental role that backscatter and reflection play in the imaging process, as well as for completeness in acoustic power and intensity studies.

To illustrate some of the issues, Fig. 9a,b displays the harmonic amplitude distributions obtained by Fourier transforming the pulse at each point in models MS1 and MS3. The transforms are smooth, as shown in Fig. 8, so that similar distributions would be found for

frequencies near the first and second harmonics. In MS1 (Fig. 9a.) the fingers, i.e., sidelobes, in the first harmonic are due to interference between the direct pulse and the edge diffractions. Standing waves are obvious in the layers. The second harmonic emerges as the pulse propagates (disregard the initial condition artifact). Note how the second harmonic develops through the tissue layers, with a sharper focus and minimal diffraction. Diffraction moves the first harmonic focus to about 4 cm, while the second harmonic focus is deeper.
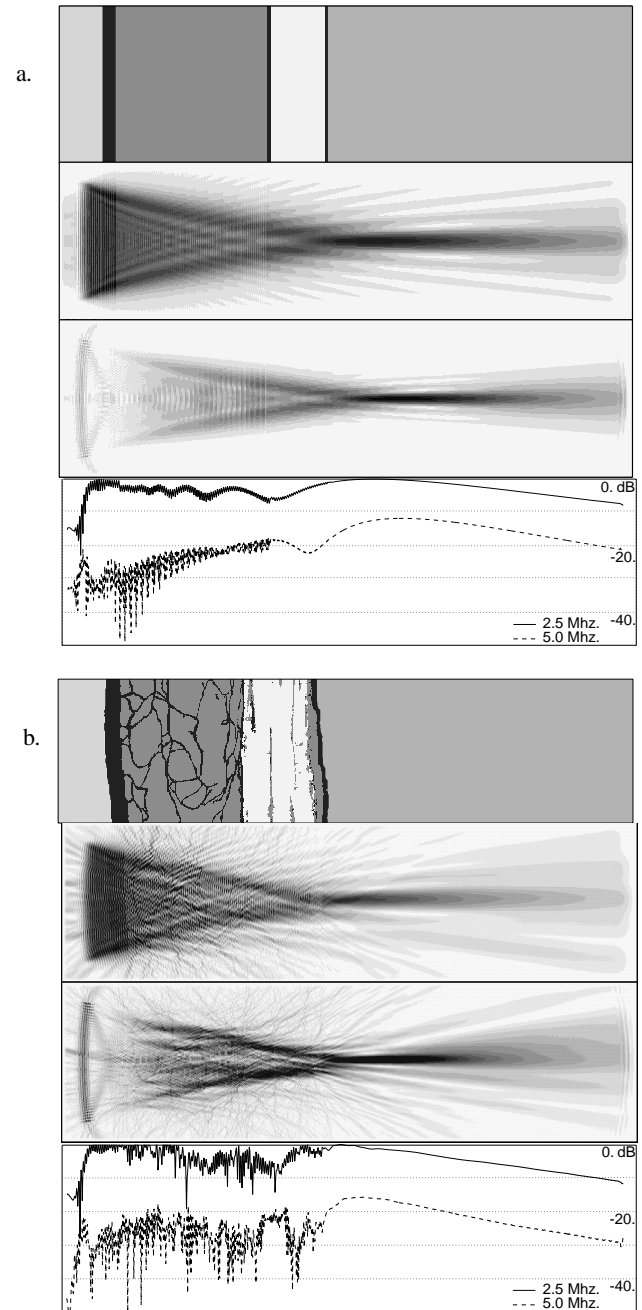
Figure 9a,b. Spectral amplitude distribution of first and second harmonic over piecewise homogeneous tissue model section (a) (MS1) and abdominal wall model section (b) (MS3) and quantified on centerline. (1.5 cm aperture and 5 cm geometric focus).

In MS3 (Fig. 9b.) there is, of course, considerable more distortion of both the first and second harmonic beams, with coherent sidelobes replaced by less coherent "feathers." The foci are not shifted laterally, although a similar plot for MS2 in Fig. 10 shows considerable focal shift, caused by fat marbling in the muscle layer. MS3 above shows less effect because the fat is more uniformly layered between the muscle and liver tissue.

These results quantify the amplitude distribution of first and second harmonic waves. Plotting the phase distribution graphically depicts the wavefront distortions, which are illustrated on the bottom of Fig. 10 for MS3. This type of study readily demonstrates the compexity of both first and second harmonic wave fields in real tissue structure, as well as the information that can be gleaned from large-scale simulations.
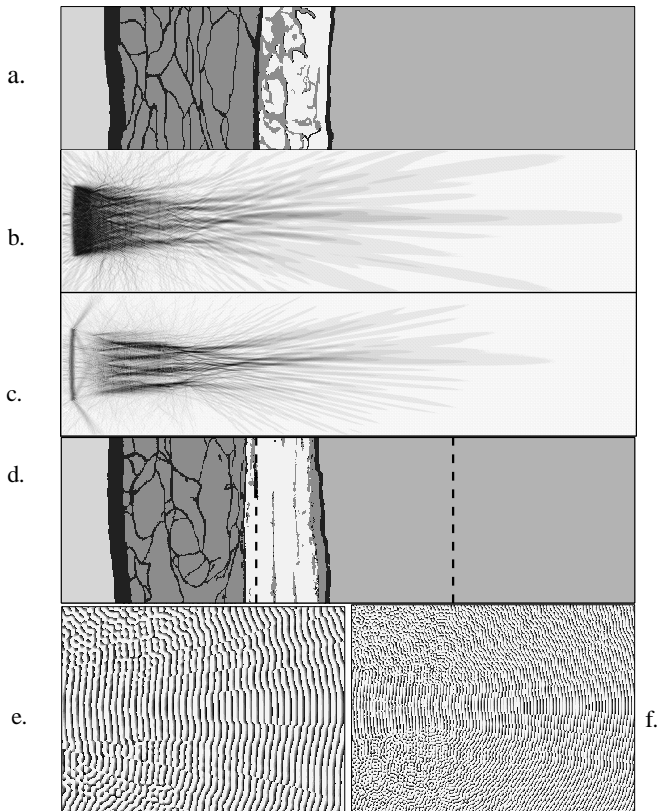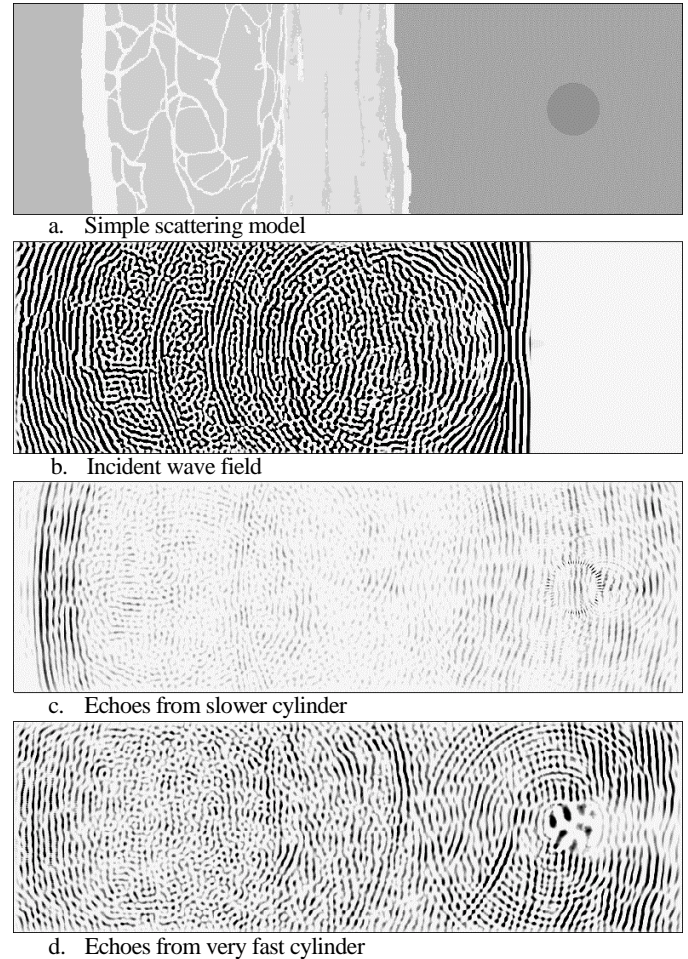

Figure 10. Panels a.,b.,c. show spectral amplitude distribution of first and second harmonic over MS2. Panels d.,e.,f. show spectral phase distribution in MS3 (d.), at 2.5 MHz (e.) and 5 MHz (f.), between the dashed lines.

CYLINDER SCATTERING AND DYNAMIC RANGE

Backscatter from deeper, coherent tissue structure is the field quantity of interest for imaging simulations. Such calculations must run long enough to propagate echoes back to the transduction region of the model. Echoes are typically weak and their calculation demands a high dynamic range, i.e., echo signal/numerical noise. Figure 11 illustrates some simple cylinder scattering examples through the MS3 abdominal section. The first picture shows a 6 mm cylinder, 5 cm from the initial wave front. The three underlying pictures are snapshots of the wave field, all at the same scale, from a transducer with 1.5 cm aperture focused on the cylinder.

The first wave snapshot in Fig. 11 shows the pressure field just before reaching the cylinder. The second shows the echo arriving in the transduction region after scattering from a soft cylinder 15% slower than the surrounding tissue. The faint cylinder outline consists of "whispering gallery" boundary waves within the slower cylinder, which persist due to total internal reflection at the interface. For a faster cylinder these modes are leaky and rapidly disappear. The third wave snapshot illustrates the case of a very hard acoustic cylinder, approximating the impedance of bone. The echoes are clearly stronger, but also less distinct in the background field because of reverberation in and leakage from the hard cylinder. This latter example suggests that the pseudospectral algorithm is robust even for very strong acoustic interfaces.

a.   Simple scattering model

b.   Incident wave field

c.   Echoes from slower cylinder

d.   Echoes from very fast cylinder

Figure 11. Simple cylinder scattering examples through the MS3 abdominal section.

Figure 12 shows examples of return signals from the slow cylinder in Fig. 11c. observed at the skin surface. The pressure history on the top is the initial pulse plus abdominal wall and cylinder reflections. Subtracting pressure history calculations with and without the cylinder yields the result on the bottom. Thus, the return is three orders of magnitude weaker than the incident field, i.e., -60 dB, which is an acceptable dynamic range. However, note the weak pressure precursor apparent at 40 microseconds. This is numerical noise, probably caused by global errors from the finite difference approximation across the cylinder interface.
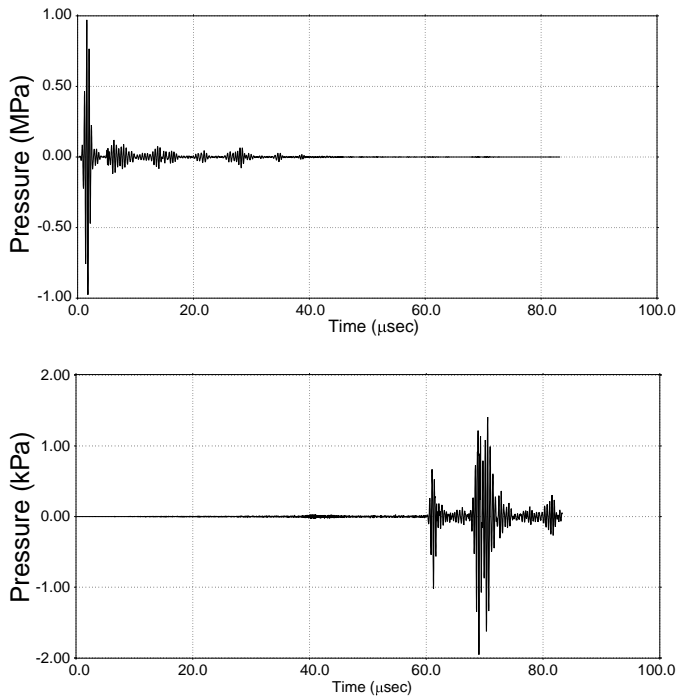
Figure 12. Examples of return signals at skin surface from the slow cylinder (Fig. 11c.). Top history shows total pressure (initial pulse plus all reflections), while bottom pressure history shows cylinder scattering only, which is three orders of magnitude lower.

CONCLUSIONS

Combining the pseudospectral (PS) method for wave solutions with the perfectly matched layer (PML) makes a formidable algorithm for large-scale ultrasound models in weakly scattering tissue. The PML is very accurate, does not cause any numerical difficulties, and the computational overhead is minor. Further reduction in problem size is offered by wave initialization on a line rather than over the domain. Generalizing to the nonlinear wave equation is straightforward and the PS method's accuracy extends the number of harmonics significantly before ringing occurs. Attenuation and dispersion models are naturally and effectively included.

Therefore, the pseudospectral wave solver is a powerful tool for studying ultrasonic pulse propagation through tissue and as an aid for imaging system evaluation. Material nonlinearity, attenuation and fine structure are accurately modeled in "long" 2D tissue cross-sections. Large scale, i.e., hundreds of wavelengths, 3D simulations require 1000x more computational resources than current PCs or workstations can provide. Massively parallel machines should yield a brute force solution to this dilemma. Fortunately, 2D simulations suffice for understanding many of the issues. Suitably combining 2D calculations in azimuth and elevation may prove useful in approximating aspects of the 3D problem.

Pulses were modeled through two abdominal wall cross-sections measured by Hinkelman and one equivalent homogeneous layered model for comparison. Fourier transforms of signals quantify second harmonic generation as the pulse propagates. The focal shifting and distortion induced by real structure relative to the baseline layered model are apparent and significant. By simulating a representative selection of tissue models, it should be possible to evaluate strategies for optimizing the second harmonic beam and aberration correction schemes, as well as estimating acoustic power levels and validating approximate schemes.

Scattering calculations demonstrate the dynamic range necessary for accurate returns from weakly (or strongly) reflecting objects 5-10 cm from the transducer. However, dynamic range needs to be increased beyond 100 dB. This can be done by continued algorithm refinements. Special attention to and treatment of material discontinuities should produce the best gains.

We conclude that rigorous transducer models can be coupled to complete tissue simulations of propagation and scattering out to many hundreds of wavelengths and back to the transducer with acceptable signal-to-noise ratio. In contrast to approximate schemes, like the KZK method, details of the field transmitted from the transducer and all backscatter on the travel path are included in the simulation. In the future, besides continued algorithm performance and accuracy enhancements, the principal challenge is to generalize these capabilities to 3D by taking advantage of massively parallel computers.

REFERENCES

1. Jensen, J.A., 1996, "Field: a program for simulating ultrasound systems," *Medical & Biological Engineering & Computing*, **34**(1-1), pp. 351-353.

2. Hayward, G., private communication, Ultrasonics Research Group, University of Strathclyde, Glasgow, Scotland.

3. Tupholme, G.E., 1969, "Generation of acoustic pulses by baffled plane pistons." *Mathematika*, **16**, pp. 209-224.

4. Stepanishen, P.R, 1971, "Transient radiation from pistons in an infinite planar baffle," *J. Acoust. Soc. Am.*, **49**, pp. 1629-1638.

5. Wojcik, G., Mould, J, Lizzi, F., Abboud, M., Ostromogilsky, M., Vaughan, D., 1995, "Nonlinear modeling of therapeutic ultrasound," *Proc. IEEE Ultrason. Symp.*, pp. 1616-1622.

6. Mast, T.D., Hinkelman, L.M., Orr, M.J., Sparrow, V.W., and Waag, R.C., 1997, "Simulation of ultrasonic pulse propagation through the abdominal wall*," J. Acoust. Soc. Am.*, **102**(2), pp. 1177-1190.

7. Wojcik, G., Fornberg, B., Waag, R., Carcione, L., Mould, J., Nikodym, L, Driscoll, T., 1997, "Pseudospectral methods for large-scale bioacoustic models," *Proc. IEEE Ultrason. Symp*., pp. 1501-1506.

8. Wojcik, G., Mould, J., Ayter, S., Carcione, L., 1998, "A study of second harmonic generation by focused medical transducer pulses," *Proc. IEEE Ultrason. Symp.*, pp. 1583-1588.

9. Fornberg, B., 1996, A Practical Guide to Pseudospectral Methods, Cambridge University Press.

10. Hinkelman, L.M., Liu, D.-L., Metlay, L.A., and Waag, R.C., 1994, "Measurements of ultrasonic pulse arrival time and energy level variations produced by propagation through abdominal wall," *J. Acoust. Soc. Am.*, **95**(1), pp. 530-541.

11. Hinkelman, L.M., Mast, T.D., Orr, M.J., and Waag, R.C., 1997, "Effects of abdominal wall morphology on ultrasonic pulse distortion," *Proc. IEEE Ultrason. Symp.*, pp. 1493-1496.

12. Chen, H-W., 1996, "Staggered-grid pseudospectral viscoacoustic wave field simulation in two-dimensional media," *J. Acoust. Soc. Am.*, **100**(1), pp. 120-132.

13. Ghrist, M., Fornberg, B., and Driscoll, T., 1998, "Staggered time integrators for wave equations," Preprint No. 394, Dept. of Applied Math., Univ. of Col., Boulder, CO.

14. Berenger, J.-P., 1994, "A perfectly matched layer for the absorption of electromagnetic waves," *J. Computational Physics*, **114**, pp. 185-200.

15. Yuan, X., Borup, D., Berggeren, M., Wiskin, J., Johnson, S., 1996, "Simulation of acoustic wave propagation in dispersive media with relaxation losses by using FDTD method with PML absorbing boundary condition," *IEEE Trans. Ultrason., Ferroelect., and Freq. Control*.

16. Carcione, J.M., Kosloff, D., Kosloff, R., 1988, "Viscoelastic wave propagation simulation in the earth," *Geophysics*, **53**(6), pp. 769-777.

17. Nachman, A., Smith, J., and Waag, R., 1990, "An equation for acoustic propagation in inhomogeneous media with relaxation losses," *J. Acoust. Soc. Am.*, **88**(3), pp. 1584-1595.

18. Szabo, T.L., 1994, "Time domain wave equations for lossy media obeying a frequency power law," *J.Acoust. Soc. Am.*, **96**(1), pp. 491-500.

19. Muir, T.G., and Carstensen, E.L., 1980, "Prediction of nonlinear acoustic effects at biomedical frequencies and intensities," *Ultrasound Med. Biol.*, **6**, pp. 345-357.

20. Furumura, T., Kennett, B.L.N., and Takenaka, H., 1998, "Parallel 3-D pseudospectral simulation of seismic wave propagation," *Geophysics,* **63**(1), pp. 279-288.

21. Duck, F.A., 1990, Physical Properties of Tissue, Academic Press.

22. Baker, Berg, A.M., Sahin, A., and Tjøtta, J.N., 1995, "The nonlinear pressure field of plane, rectangular apertures: Experimental and theoretical results*," J. Acoust. Soc. Am.*, **97**, pp. 3510-3517.

23. Averkiou, M.A., and Hamilton, M.F., 1997, "Nonlinear distortion of short pulses radiated by plane and focused circular pistons," *J. Acoust. Soc. Am.*, **102**.

24. Powell, D.J., Wojcik, G.L., Desilets, C.S., Gururaja, T.R., Guggenberger, K., Sherrit, S., and Mukherjee, B.K., 1997, "Incremental "Model-build-test" validation exercise for a 1-D biomedical ultrasonic imaging array," *Proc. IEEE Ultrason. Symp.*, pp. 1669 1674.